Magn Reson Med Sci 2023; 22; 67–78
doi:10.2463/mrms.mp.2021-0123 Published Online: January 26, 2022

MAJOR PAPER

Correlation between Phase-difference-enhanced MR Imaging and Amyloid Positron Emission Tomography: A Study on Alzheimer's Disease Patients and Normal Controls

Hirotaka Takita[1], Satoshi Doishita[1,2], Tetsuya Yoneda[3], Hiroyuki Tatekawa[1*], Takato Abe[4,5], Yoshiaki Itoh[5], Daisuke Horiuchi[1], Taro Tsukamoto[1], Taro Shimono[1], and Yukio Miki[1]

Purpose: While amyloid-β deposition in the cerebral cortex for Alzheimer's disease (AD) is often evaluated by amyloid positron emission tomography (PET), amyloid-β-related iron can be detected using phase difference enhanced (PADRE) imaging; however, no study has validated the association between PADRE imaging and amyloid PET. This study investigated whether the degree of hypointense areas on PADRE imaging correlated with the uptake of amyloid PET.

Methods: PADRE imaging and amyloid PET were performed in 8 patients with AD and 10 age-matched normal controls. ROIs in the cuneus, precuneus, superior frontal gyrus (SFG), and superior temporal gyrus (STG) were automatically segmented. The degree of hypointense areas on PADRE imaging in each ROI was evaluated using 4-point scaling of visual assessment or volumetric semiquantitative assessment (the percentage of hypointense volume within each ROI). The mean standardized uptake value ratio (SUVR) of amyloid PET in each ROI was also calculated. The Spearman's correlation coefficient between the 4-point scale of PADRE imaging and SUVR of amyloid PET or between the semiquantitative hypointense volume percentage and SUVR in each ROI was evaluated.

Results: In the precuneus, a significant positive correlation was identified between the 4-point scale of PADRE imaging and SUVR of amyloid PET (Rs = 0.5; $P = 0.034$) in all subjects. In the cuneus, a significant positive correlation was identified between the semiquantitative volume percentage of PADRE imaging and SUVR of amyloid PET (Rs = 0.55; $P = 0.02$) in all subjects.

Conclusion: Amyloid-β-enhancing PADRE imaging can be used to predict the SUVR of amyloid PET, especially in the cuneus and precuneus, and may have the potential to be used for diagnosing AD by detecting amyloid deposition.

Keywords: *Alzheimer's disease, amyloid positron emission tomography, phase difference enhanced imaging*

Introduction

Numerous studies have reported that deposition of amyloid-β in the cerebral cortex is one of the earliest neuropathological events in Alzheimer's disease (AD), occurring decades before symptom onset.[1,2] Non-invasive examination for early detection of amyloid-β deposition is considered to be important for early diagnosis of AD.

Amyloid positron emission tomography (PET), using ^{11}C-Pittsburgh compound B (^{11}C-PiB) or other ^{11}C/^{18}F tracers, can visualize the deposition of amyloid-β in the human cerebral cortex and has been rapidly adopted worldwide.[3–8] However, when patients are suspected of having AD, amyloid PET is not routinely performed due to radiation exposure, limited availability of PET systems, and relatively high costs. Meanwhile, several histopathological studies of AD

[1]Department of Diagnostic and Interventional Radiology, Graduate School of Medicine, Osaka City University, Osaka, Osaka, Japan
[2]Department of Radiology, Saitama Red Cross Hospital, Saitama, Saitama, Japan
[3]Department of Medical Physics in Advanced Biomedical Sciences, Faculty of Life Sciences, Kumamoto University, Kumamoto, Kumamoto, Japan
[4]Department of Neurology, Tokai University School of Medicine, Isehara, Kanagawa, Japan
[5]Department of Neurology, Graduate School of Medicine, Osaka City University, Osaka, Osaka, Japan

*Corresponding Author: Department of Diagnostic and Interventional Radiology, Graduate School of Medicine, Osaka City University, 1-4-3, Asahi-machi, Abeno-ku, Osaka, Osaka 545-8585, Japan. Phone: +81-6-6645-3831, Fax: +81-6-6646-6655, Email: htatekawa@med.osaka-cu.ac.jp

Received: September 8, 2021 | Accepted: November 24, 2021

reported that iron colocalized with amyloid-β in the cerebral cortex of postmortem AD patients and transgenic mice with AD,[9–12] and such iron was detected non-invasively using MRI without radiation exposure. Some previous studies attempted to visualize amyloid-β-related iron deposition using T2*-weighted imaging,[13,14] susceptibility-weighted imaging (SWI),[15] or quantitative susceptibility mapping (QSM) sequences.[16,17] Among them, QSM was often compared with amyloid PET and was expected to predict amyloid deposition.[18–21] Although some studies reported significant associations between the susceptibility calculated by QSM and the standardized uptake value ratio (SUVR) calculated by amyloid PET in the cerebral cortex of patients with AD,[18,19] others did not show associations between them.[20,21] Such a discrepancy might be due to the fact that the susceptibility calculated by QSM represented not only amyloid-β-related iron but also other high-susceptibility substances, including age-related iron.[20,21] QSM, however, cannot differentiate amyloid-β-related iron from age-related iron, which may limit the use of the QSM sequence.

Phase difference enhanced (PADRE) imaging was developed,[22] and this phase-weighted MRI technique enhanced phase differences between the target and the surrounding tissue to visualize the target tissue. Using this technique, some studies differentiated pathologies of central nervous system disease[23] and detected early pathological changes in some types of neurodegenerative diseases, including multiple sclerosis,[24] multiple system atrophy,[22] amyotrophic lateral sclerosis,[25] and corticobasal syndrome.[26] Recently, Yoneda et al.[27] have developed a new technique of PADRE imaging, which extracts only amyloid-β-related iron from all types of iron using phase differences, and succeeded in highlighting amyloid-β-related iron deposition as hypointense areas on PADRE imaging in the cerebral cortex of transgenic mice with AD. These hypointense areas were consistent with the distribution of amyloid-β in histopathological analysis.[27] Tateishi et al.[28] visually assessed hypointense areas of the human brain on amyloid-β-enhancing PADRE imaging and identified more remarkable hypointense areas in the cerebral cortex of patients with AD compared with normal controls (NCs).

However, to date, no study has evaluated the correlation between PADRE imaging and amyloid PET. We hypothesize that the degree of hypointense areas detected on PADRE imaging might correlate with the uptake of amyloid PET. Therefore, the aim of this study was to investigate whether the degree of hypointense areas on PADRE imaging correlated with the SUVR of amyloid PET, and whether PADRE imaging has the potential to be used for diagnosing AD.

Materials and Methods

Subjects

Because this is an exploratory study, to make the correlation between uptakes of amyloid PET and amyloid-β-enhancing PADRE imaging clear, we recruited AD patients with amyloid PET positive and NCs with amyloid PET negative. The inclusion criteria for patients with AD were as follows: 1) patients who were suspected of having dementia at the Department of Neurology at our institution and underwent MRI and ^{11}C-PiB PET between January 2015 and April 2018; 2) patients who met the diagnostic criteria of probable or possible AD established by the National Institute of Neurological and Communicative Disorders and Stroke and the Alzheimer's Disease and Related Disorders Association (NINCDS-ADRDA);[29] and 3) patients who were diagnosed with ^{11}C-PiB PET positive. Finally, eight patients (three patients retrospectively and five patients prospectively) were included and classified into the AD group. In contrast, age-matched, 11 NCs were prospectively recruited from the advertisements between August 2016 and February 2017. Experienced neurologists confirmed their cognitive function using the Mini-Mental State Examination (MMSE) scores, and the medical history was unremarkable. The NCs also underwent MRI and ^{11}C-PiB PET. One NC who was with ^{11}C-PiB PET positive was excluded. Finally, 10 NCs were included and classified into the NC group. A flowchart of the inclusion and exclusion criteria for this study is presented in Fig. 1. This study was approved by our institutional review board. Written informed consent was obtained from all the participants.

MRI protocol

MRI was performed using a 3T system (Ingenia; Philips Healthcare, Best, the Netherlands) with a 32-channel head coil. Volumetric images were obtained in the sagittal plane with the following parameters: 3D T1-turbo field echo (TFE) sequence, TR = 5.45–5.69 ms, TE = 2.43–2.55 ms, flip angle (FA) = 9°, number of sample averaged (NSA) = 1, FOV = 256 × 256 mm, matrix = 256 × 256, and slice thickness = 1 mm without a gap. PADRE images were obtained in the axial plane parallel to the anterior commissure-posterior commissure line with the following parameters: 3D multi-echo gradient echo SWI-phase sequence; TR = 31 ms; TE = 7.2, 13.4, 19.6, and 25.8 ms; FA = 17°; NSA = 1; FOV = 230 × 230 mm; matrix = 640 × 640, 672 × 672, or 768 × 768; slice thickness = 1 mm without a gap. Phase unwrapping (high-pass filter with kernel size = 160 × 160 or 192 × 192) was applied to all datasets using MATLAB (R2018a; MathWorks, Natick, MA, USA).

Drawing ROIs on PADRE images

In this study, we set automated segmentation to extract target ROIs using automated anatomical labeling (AAL) 2nd version atlas in the Montreal Neurological Institute (MNI) standard brain with MATLAB and statistical parametric mapping 12 software (SPM12; Wellcome Trust Centre for Neuroimaging, London, UK).[30] An overview is shown in Supplementary Figs. 1 and 2. 3D T1-TFE images were segmented into gray matter (GM), white matter (WM), and

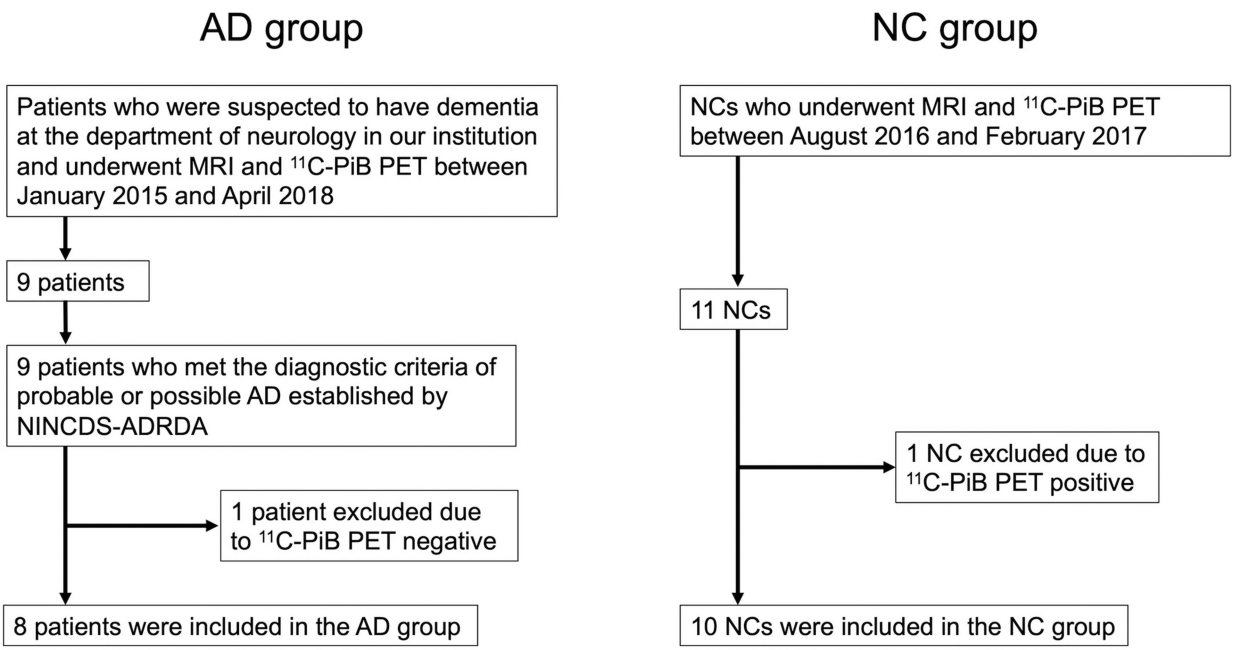

Fig. 1 A flowchart of inclusion and exclusion criteria. AD, Alzheimer's disease; ^{11}C-PiB, ^{11}C-Pittsburgh compound B; NC, normal control; NINCDS-ADRDA, National Institute of Neurological and Communicative Disorders and Stroke and the Alzheimer's Disease and Related Disorders Association; PET, positron emission tomography.

a tissue probability map (TPM) corresponding to the segmented GM was obtained. The brain atlas in the MNI space (TPM of GM of the atlas) was warped into the individual native space (individual TPM of GM) using nonlinear registration, creating a translation matrix. The AAL brain atlas map in the MNI space was then warped nonlinearly into the individual native space by applying the translation matrix with the nearest-neighbor interpolation. The deformed AAL brain atlas map and deformed TPM of GM were resliced to fit the dimensions of the native space. By applying a threshold of probability = 0.7 to the deformed TPM of GM, an individual GM mask was created. We created an AAL atlas-based GM ROI by overlaying the GM mask on the deformed AAL brain atlas map. This AAL atlas-based GM ROI partially contained WM and vessels, which might give an unwanted phase in the histogram while analyzing PADRE imaging. Thus, we eliminated them by additionally applying WM and vessel masks to the ROI as follows: first, we reconstructed PADRE images by selecting the phases of the WM and vessel at different TEs of 7.2, 13.4, 19.6, and 25.8 ms. Second, we averaged them over all PADRE images in different TEs with weights of 1:2:9:16. This weighting procedure resulted in a higher signal from short TE components and phase contrast from long TE components, and averaging also realized a decrease in image noise, resulting in the creation of high-contrast noise ratio images. Third, a bias correction was applied to the PADRE images, and the averaged signal (AS) and standard deviation (SD) of the cortex in PADRE images were measured to binarize the PADRE image by setting the threshold AS – SD, creating a WM and vessel mask (PADRE mask).[22,31] Finally, regions of WM and vessels (PADRE mask) were removed from the AAL atlas-based GM ROI, creating a definitive atlas-based GM ROI. According to a previous PADRE study,[28] this study selected specific brain regions, namely, the cuneus, precuneus, superior frontal gyrus (SFG), and superior temporal gyrus (STG), as target cortex ROIs for the following examination.

Quantitative evaluation of PADRE images

We assumed that the phase of the cerebral cortex could be classified into the following two types of iron: age-related iron and amyloid-β-related iron. To enhance the phase difference, a double Gaussian distribution model was applied according to a previous study.[28] Based on the central limit theorem, the phase distributions of age-related iron and amyloid-β-related iron showed different Gaussian distributions. Following the above assumptions, we fit the phase distribution in the target ROIs, including the cortex of the cuneus, precuneus, SFG, and STG, for each subject with the sum of two Gaussian curves D(θ):[28]

$$D(\theta) = A_1 e^{-a_1(\theta - b_1)^2} + A_2 e^{-a_2(\theta - b_2)^2},$$

where $A_1 e^{-a_1(\theta - b_1)^2}$ is a Gaussian distribution representing the phase of age-related iron with real parameters A_1, a_1, and b_1, and $A_2 e^{-a_2(\theta - b_2)^2}$ is a Gaussian distribution

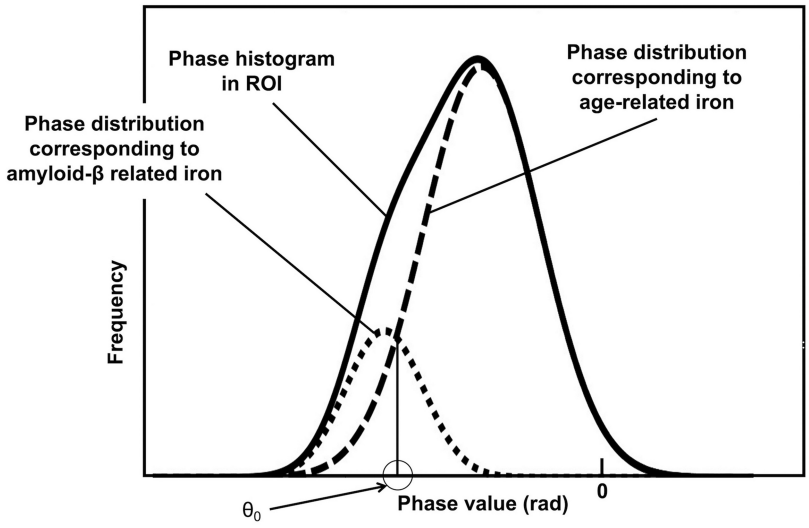

Fig. 2 A model figure of double Gaussian fitting to a phase value histogram. The horizontal axis indicates the phase value, and the vertical axis indicates the frequency (number of counts) at each phase value. Phase data (solid line) is fitted by double Gaussians; age-related iron (dashed line) and amyloid-β-related iron (dotted line). The intersection (θ_0) is numerically derived by fitted parameters for each subject.

representing the phase of amyloid-β-related iron with real parameters A_2, a_2, and b_2. In this model, we set the initial parameters to fit A_1, a_1, b_1, A_2, a_2, and b_2 as the peak value of phase distribution, square of SD of phase distribution, phase value of peak of phase distribution, one-quarter of peak value of phase distribution, a_1 – 0.1 rad, and b_1 – 0.1 rad, respectively, for individual echo data. Figure 2 shows a model of double Gaussian fitting to a phase-value histogram. The horizontal axis indicates the phase value, while the vertical axis indicates the frequency (number of counts) at each phase value. Phase data (solid line) are fitted by double Gaussians distribution: age-related iron (dashed line) and amyloid-β-related iron (dotted line). The intersection (θ_0) is numerically derived using the fitted parameters for each subject. In this study, PADRE imaging would select a phase band below θ_0 to enhance amyloid-β-related iron.

We derived the intersections in each cortex with GM ROIs and enhanced the phase band below the intersections by reconstructing the PADRE. This was due to the reason that age-related and amyloid-β-related iron depositions differed depending on the brain regions,[32] and, therefore, the intersection of the double Gaussian curve may differ among brain regions. After determining the threshold, which appropriately enhanced amyloid-β-related iron deposition, with respect to the cuneus, precuneus, SFG, and STG, we finally created four amyloid-β-enhancing PADRE images corresponding to each brain region (the cuneus, precuneus, SFG, and STG). We used the abovementioned four amyloid-β-enhancing PADRE images by each subject for the following qualitative and semiquantitative evaluations.

Qualitative evaluation of PADRE Images

Two neuroradiologists (6 and 10 years of clinical experience), who were blinded to the information of all participants, independently assessed the hypointense areas of the cuneus, precuneus, SFG, and STG on the corresponding amyloid-β-enhancing PADRE imaging. According to a previous study,[28] a 4-point scale was used as follows: grade 1, almost no hypointense foci in the cortex; grade 2, sparse distribution of hypointense foci in the cortex; grade 3, intermediate distribution of hypointense foci in the cortex; and grade 4, extensive distribution of hypointense foci in the cortex (Fig. 3). When the laterality of the cortex signal was observed, we chose the cortex with more remarkable signal changes. When discrepancies occurred between the two readers, a consensus was reached on the final scale.

Volumetric semiquantitative evaluation of PADRE Images

An example of the 4-point scale and semiquantitative evaluation is shown in Fig. 4. The volume percentage of hypointense areas within the ROIs of the cuneus, precuneus, SFG, and STG was semi-quantitatively calculated as follows: 1) a neuroradiologist (6 years of clinical experience) visually and randomly chose 20 pixels in the hypointense areas within each ROI using the ITK-SNAP software (PICSL, Philadelphia, PA, USA; www.itksnap.org); 2) the thresholds of hypointense areas within each ROI were determined as a range from the lowest to the highest intensity of 20 pixels chosen randomly; 3) the hypointense mask within each ROI was created by the thresholds visually determined using the Analysis of Functional NeuroImages software (AFNI, *3dcalc*; NIMH Scientific and Statistical Computing Core; Bethesda, MD, USA; https://afni.nimh.nih.gov) (Fig. 4c and 4g); 4) the volume of the hypointense mask within each ROI was calculated using AFNI (*3dBrickStat*) and defined as the hypointense volume within each ROI; 5) the volume of each ROI was also calculated using AFNI (*3dBrickStat*); and 6) the volume percentage of hypointense areas within each ROI was calculated.

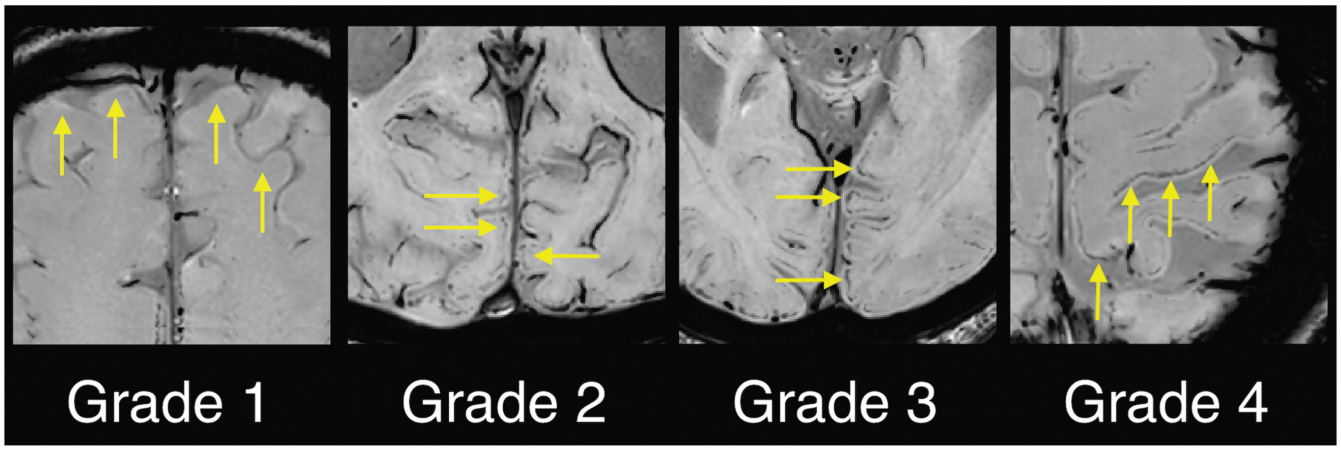

Fig. 3 A 4-point scale of visual assessment of PADRE imaging: grade 1, almost no hypointense area in the cortex (arrows); grade 2, sparse distribution of hypointense area in the cortex (arrows); grade 3, intermediate distribution of hypointense area in the cortex (arrows); grade 4, dense distribution of hypointense area in the cortex (arrows). PADRE, phase difference enhanced.

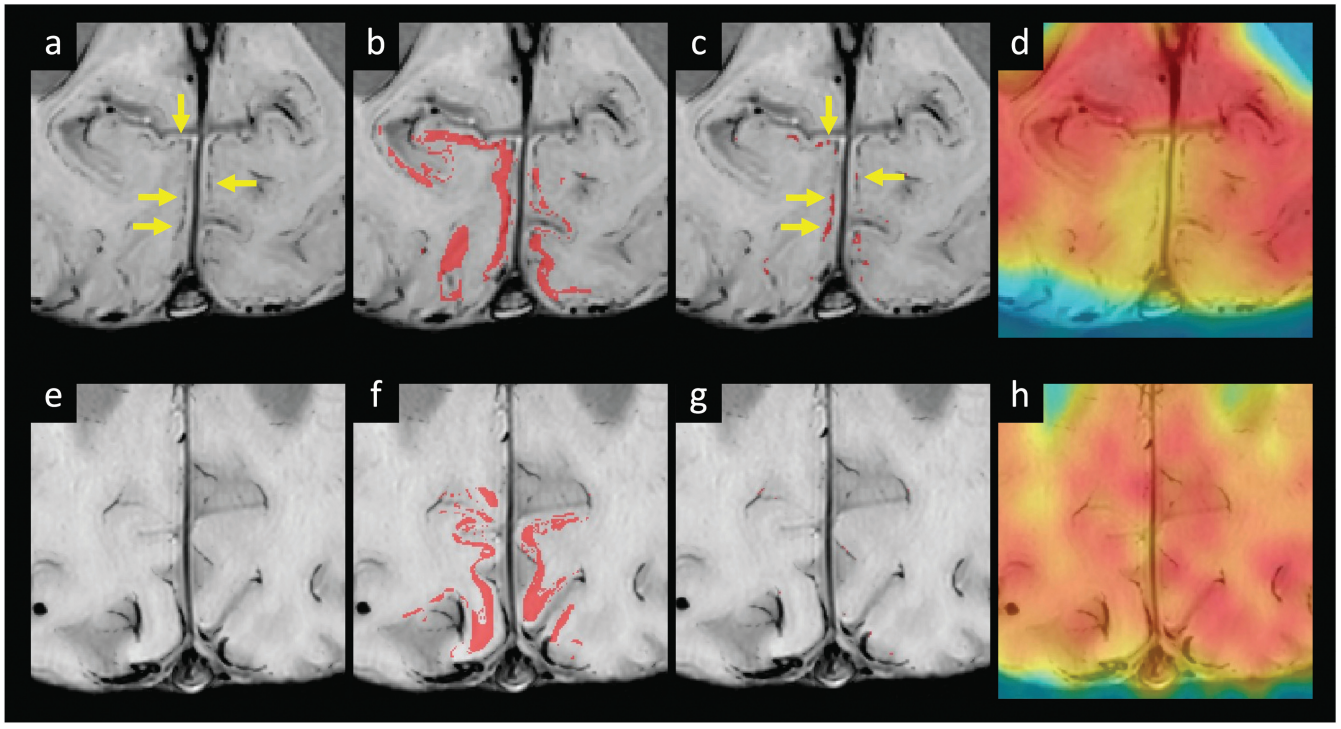

Fig. 4 An example of the 4-point scale and semiquantitative evaluation. The upper row (**a**–**d**) shows a subject with AD, whose SUVR of amyloid PET is well correlated with the 4-point scale and the semiquantitative hypointense volume percentage of PADRE images. The lower row (**e**–**h**) shows another subject with AD, whose SUVR of amyloid PET is not well correlated with the 4-point scale and the semiquantitative hypointense volume percentage of PADRE images. (**a**) is the cuneus of the PADRE image, and the arrows show linear hypointense areas with grade 3 of the 4-point scale. (**b**) is the same level as that of (**a**) in the PADRE image, and the red areas show AAL atlas-based cuneus ROI. (**c**) is the same level as that of (**a**) in the PADRE image, and the red areas show the hypointense mask determined by the semiquantitative evaluation. The semiquantitative hypointense volume percentage of this subject is 8.02%. (**d**) is the same level as that of (**a**) in amyloid PET and shows high uptake of the tracer in the cuneus. The mean SUVR in the cuneus of this subject is 1.44. (**e**) is the precuneus of the PADRE image and shows almost no hypointense areas with grade 1 of the 4-point scale. (**f**) is the same level as that of (**e**) in the PADRE image, and the red areas show AAL atlas-based precuneus ROI. (**g**) is the same level as that (**e**) of the PADRE image, and the red areas show the hypointense mask determined by the semiquantitative evaluation. The semiquantitative hypointense volume percentage of this subject is 1.16%. (**h**) is the same level as that of (**e**) in amyloid PET and shows high uptake of the tracer in the precuneus. The mean SUVR in the cuneus of this subject is 1.91.

Table 1 Summary of clinical data.

	Total (n = 18)	AD group (n = 8)	NC group (n = 10)	*P* value
Female	8 (44.4%)	3 (37.5%)	5 (50%)	0.66[a]
Median age (IQR) (year)	74 (69, 81)	74 (70, 77)	74 (68, 81)	0.72[b]
Median MMSE (IQR)	28.5 (22.75, 29.75)	21.5 (17.5, 26.25)	29 (28.25, 29.75)	0.004[b*]

[a]Using Fisher's exact test. [b]Using Mann–Whitney U test. *Indicating a statistical significance. AD, Alzheimer's disease; IQR, interquartile range; MMSE, mini-mental state examination; NC, normal control; SD, standard deviation.

Acquisition of ^{11}C-PiB PET and calculation of SUVR

^{11}C-PiB PET scans were performed using an Eminence-B/SET-3000B (Shimadzu, Kyoto, Japan) camera. Participants were injected with 330–570 MBq of ^{11}C-PiB, and then scanned using a dynamic acquisition that lasted for 50–70 min. Reconstruction of ^{11}C-PiB images was performed by filtered back projection using a 5-mm full width at half maximum Gaussian filter with attenuation and scatter correction. Then, SUVR maps were reconstructed with the midbrain as a reference region using the frame summation of dynamics of the image for 50 to 70 min after ^{11}C-PiB injection using PMOD software (version 3.7; PMOD Technologies, Zurich, Switzerland).[33] The SUVR maps were registered to the individual native space of MRI using a 6-degree-of-freedom rigid transformation and a mutual information cost function using FSL software (FLIRT, version 6.0; FMRIB, Oxford, UK; http://www.fmrib.ox.ac.uk/fsl/). The definitive atlas-based GM ROI was applied to each SUVR map, and the mean SUVR within each ROI was recorded using the ITK-SNAP software.

Statistical analysis

Statistical analyses of differences between the AD and NC groups were performed using Fisher's exact test for sex ratio and Mann–Whitney U test for differences in age, MMSE, 4-point scale, semiquantitative volume percentage, and SUVR. The Spearman's rank correlation coefficients among the 4-point scale of PADRE images, semiquantitative volume percentage, and SUVR of amyloid PET in each ROI (cuneus, precuneus, SFG, and STG) were calculated. Weighted kappa coefficients with quadratic weights were calculated to assess the inter-rater agreement between the two neuroradiologists. The 4-point scale, semiquantitative volume percentage, and SUVR were also compared among the ROIs for the AD or NC group alone using the Mann–Whitney U test with the Benjamini–Hochberg method for multiple comparison corrections. In the AD or NC group alone, Spearman's rank correlation coefficients among the 4-point scale of PADRE images, semiquantitative volume percentage, and SUVR of amyloid PET in each ROI were also calculated using the Benjamini–Hochberg method for multiple comparison corrections. Statistical significance was set at $P < 0.05$. Statistical analyses were performed using R software (version 3.5.2; http://www.r-project.org/) and GraphPad Prism (Version 8.3; GraphPad Software, San Diego, CA, USA).

Results

Clinical data

The subjects' characteristics are shown in Table 1. The AD group included 8 subjects (female, 3; median age, 74 years; median MMSE, 21.5), and the NC group included 10 subjects (female, 5; median age, 74 years; median MMSE, 29). No significant differences were identified in sex ($P = 0.66$) or age ($P = 0.72$) between the AD and NC groups. The MMSE score of the AD group was significantly lower than that of the NC group ($P = 0.004$).

Visual assessment of PADRE imaging

A summary of the 4-point scale of the PADRE images is presented in Table 2. In the AD group, the mean grades of the cuneus, precuneus, SFG, and STG were 2.37, 1.75, 2.25, and 1.25, respectively (median: 2.5, 2, 2.5, and 1, respectively). In the NC group, the mean grades of the cuneus, precuneus, SFG, and STG were 1.9, 1.3, 2.2, and 1.5, respectively (median: 2, 1, 2, and 1, respectively). In all ROIs, no significant differences were identified between the AD and NC groups in the 4-point scale (cuneus, $P = 0.19$; precuneus, $P = 0.15$; SFG, $P = 0.88$; STG, $P = 0.48$). The inter-rater agreement was good (weighted kappa coefficient = 0.63). The 4-point scale showed no significant differences in any pairs of brain regions within either group.

Semiquantitative assessment of PADRE imaging

A summary of the semiquantitative evaluation of the PADRE images is presented in Table 3. In the AD group, the mean semiquantitative volume percentages of the cuneus, precuneus, SFG, and STG were 5.08, 4.17, 2.74, and 1.86, respectively (median: 5.16, 4.45, 2.59, and 1.5, respectively). In the NC group, the mean semiquantitative volume percentage of the cuneus, precuneus, SFG, and STG were 2.41, 1.92, 2.02, and 1.56, respectively (median: 2.69, 1.68, 2.32, and 1.71, respectively). In the cuneus and precuneus, the semiquantitative volume percentage of the AD group was significantly higher than that of the NC group (cuneus, $P = 0.002$; precuneus, $P = 0.02$). In the SFG and STG, no significant differences were identified between the semiquantitative volume percentage of

Table 2 Summary of a 4-point scale of PADRE images.

		AD group (n = 8)	NC group (n = 10)	*P* value
Cuneus	Grade 1	1/8 (12.5)	3/10 (30)	
	Grade 2	3/8 (37.5)	5/10 (50)	
	Grade 3	4/8 (50)	2/10 (20)	
	Grade 4	0/8 (0)	0/10 (0)	
	Mean (SD)	2.37 (0.74)	1.9 (0.73)	0.19[a]
Precuneus	Grade 1	3/8 (37.5)	7/10 (70)	
	Grade 2	4/8 (50)	3/10 (30)	
	Grade 3	1/8 (12.5)	0/10 (0)	
	Grade 4	0/8 (0)	0/10 (0)	
	Mean (SD)	1.75 (0.7)	1.3 (0.48)	0.15[a]
SFG	Grade 1	2/8 (25)	2/10 (20)	
	Grade 2	2/8 (25)	4/10 (40)	
	Grade 3	4/8 (50)	4/10 (40)	
	Grade 4	0/8 (0)	0/10 (0)	
	Mean (SD)	2.25 (0.88)	2.2 (0.78)	0.88[a]
STG	Grade 1	6/8 (75)	6/10 (60)	
	Grade 2	2/8 (25)	3/10 (30)	
	Grade 3	0/8 (0)	1/10 (10)	
	Grade 4	0/8 (0)	0/10 (0)	
	Mean (SD)	1.25 (0.46)	1.5 (0.7)	0.48[a]

[a]Using Mann–Whitney U test. AD, Alzheimer's disease; NC, normal control; PADRE, phase difference enhanced; SD, standard deviation; SFG, superior frontal gyrus; STG, superior temporal gyrus.

Table 3 Summary of semiquantitative volume percentage of hypointense areas within each ROI of the PADRE images.

	AD group (n = 8)	NC group (n = 10)	*P* value
Cuneus	5.08 (1.57)	2.41 (1.21)	0.002[a*]
Precuneus	4.17 (2.02)	1.92 (0.71)	0.02[a*]
SFG	2.74 (1.35)	2.02 (1.16)	0.48[a]
STG	1.86 (1.61)	1.56 (0.66)	0.97[a]

Data are mean with standard deviation in parentheses. [a]Using Mann–Whitney U test. *Indicating a statistical significance. AD, Alzheimer's disease; NC, normal control; PADRE, phase difference enhanced; SFG, superior frontal gyrus; STG, superior temporal gyrus.

the AD and NC groups (SFG, $P = 0.48$; STG, $P = 0.97$). In the AD group, the semiquantitative volume percentage in the cuneus was significantly higher than that in SFG ($P = 0.026$) and STG ($P = 0.01$), while in the NC group, there were no significant differences in any pairs of brain regions.

SUVR of amyloid PET in each ROI

A summary of the SUVR of amyloid PET in each ROI is presented in Table 4. In the AD group, the mean SUVR of the cuneus, precuneus, SFG, and STG were 1.49, 1.92, 1.75, and 1.62, respectively. In the NC group, the mean SUVR of the cuneus, precuneus, SFG, and STG were 1.14, 1.12, 1.14, and 1.1, respectively. In either pair of regions, the SUVR was significantly higher in the AD group than in the NC group (all $Ps < 0.001$). For the AD group, the SUVR in the precuneus was significantly higher than that in the cuneus ($P = 0.002$) and STG ($P = 0.02$), and the SUVR in the cuneus was significantly lower than that in the SFG ($P = 0.029$). For the NC group, SUVR did not showed significant differences in any pairs of brain regions.

Table 4 Summary of SUVR of amyloid PET in each ROI.

	AD group (n = 8)	NC group (n = 10)	*P* value
Cuneus	1.49 (0.15)	1.14 (0.05)	< 0.001[a*]
Precuneus	1.92 (0.17)	1.12 (0.06)	< 0.001[a*]
SFG	1.75 (0.18)	1.14 (0.11)	< 0.001[a*]
STG	1.62 (0.17)	1.1 (0.05)	< 0.001[a*]

Data are mean with standard deviation in parentheses. [a]Using Mann–Whitney U test. *Indicating a statistical significance. AD, Alzheimer's disease; NC, normal control; PET, positron emission tomography; SFG, superior frontal gyrus; STG, superior temporal gyrus; SUVR, standardized uptake value ratio.

Correlation between PADRE imaging and SUVR of amyloid PET

The correlations between the 4-point scale of PADRE images and SUVR of amyloid PET and between the semiquantitative volume percentage and SUVR are shown in Fig. 5. In the precuneus, a significant positive correlation was identified between the 4-point scale of PADRE images and SUVR of amyloid PET (Rs = 0.5, P = 0.034). In the cuneus, SFG or STG, no significant correlations were identified between the 4-point scale of PADRE images and SUVR of amyloid PET (cuneus, Rs = 0.106, P = 0.67; SFG, Rs = –0.024, P = 0.92; STG, Rs = −0.44, P = 0.064). When evaluating the correlation coefficient using the AD or NC group alone, no significant correlations were identified.

In the cuneus, a significant positive correlation was identified between the semiquantitative volume percentage of PADRE images and SUVR of amyloid PET (Rs = 0.55, P = 0.02) in all subjects. In the precuneus, SFG, and STG, no significant correlations were identified between the semiquantitative volume percentage and SUVR of amyloid PET (precuneus, Rs = 0.43, P = 0.07; SFG, Rs = –0.07, P = 0.77; STG, Rs = −0.2, P = 0.43). No significant correlations were identified using the AD or NC group alone.

The correlation between the 4-point scale and semiquantitative volume percentage of the PADRE images is shown in Supplementary Fig. 3.

Discussion

This study showed a significant positive correlation between the 4-point scale of amyloid-β-enhancing PADRE imaging and SUVR of amyloid PET in the precuneus and between the semiquantitative volume percentage of PADRE imaging and SUVR in the cuneus, although no correlations between them were identified in the SFG or STG. This study suggested that amyloid-β-enhancing PADRE imaging in the cuneus and precuneus could be used to predict the SUVR of amyloid PET.

The difference in our results of the correlation among the 4-point scale, semiquantitative volume percentage, and SUVR depending on each ROI may be multifactorial. Several studies on amyloid PET for AD reported that the mean SUVR in the precuneus was higher than that in the cuneus, SFG, and STG,[34,35] and that the amyloid PET ligands accumulated from an earlier phase of AD in the precuneus compared with the cuneus, SFG, and STG.[36] Similar to these previous studies, this study showed that the mean SUVR in the precuneus showed the highest value and was significantly higher than that in the cuneus and STG. Hence, the significant positive correlation between the 4-point scale and SUVR in the precuneus may be due to the higher number of amyloid plaques in the precuneus than in the cuneus, SFG, and STG. However, it is unlikely that only the number of amyloid plaques affects the results of the correlation between amyloid-β-enhancing PADRE imaging and amyloid PET since the cuneus, whose mean SUVR of amyloid PET was the lowest among each ROI, showed a significant positive correlation between the semiquantitative volume percentage of PADRE imaging and SUVR of amyloid PET. Some studies reported that the cortical iron was deposited in amyloid plaques, tau tangles, and activated microglia in AD.[37–42] This tau tangles-related iron and activated microglia-related iron may affect our results regarding the correlation between amyloid-β-enhancing PADRE imaging and amyloid PET. However, to our knowledge, no study has reported the difference in tau tangles-and activated microglia-related iron deposits depending on the brain region. Thus, further investigation is needed.

Unlike QSM evaluation, amyloid-β-enhancing PADRE images can stratify amyloid-β-related iron from age-related iron by evaluating phase differences, which is an advantage of PADRE imaging. In this study, the substances at a lower phase than the intersection (θ_0) of the double Gaussian distribution were enhanced as hypointense areas, assuming as amyloid-β-related iron. This mathematical stratification method can unbiasedly extract deposition of amyloid-β-related iron; however, this method requires further improvement because the optimization of iron stratification may differ depending on the amount of the deposition of amyloid-β-related, age-related, tau tangles-related, and activated microglia-related iron or the parameters of PADRE sequences. The detection accuracy of amyloid-β-related

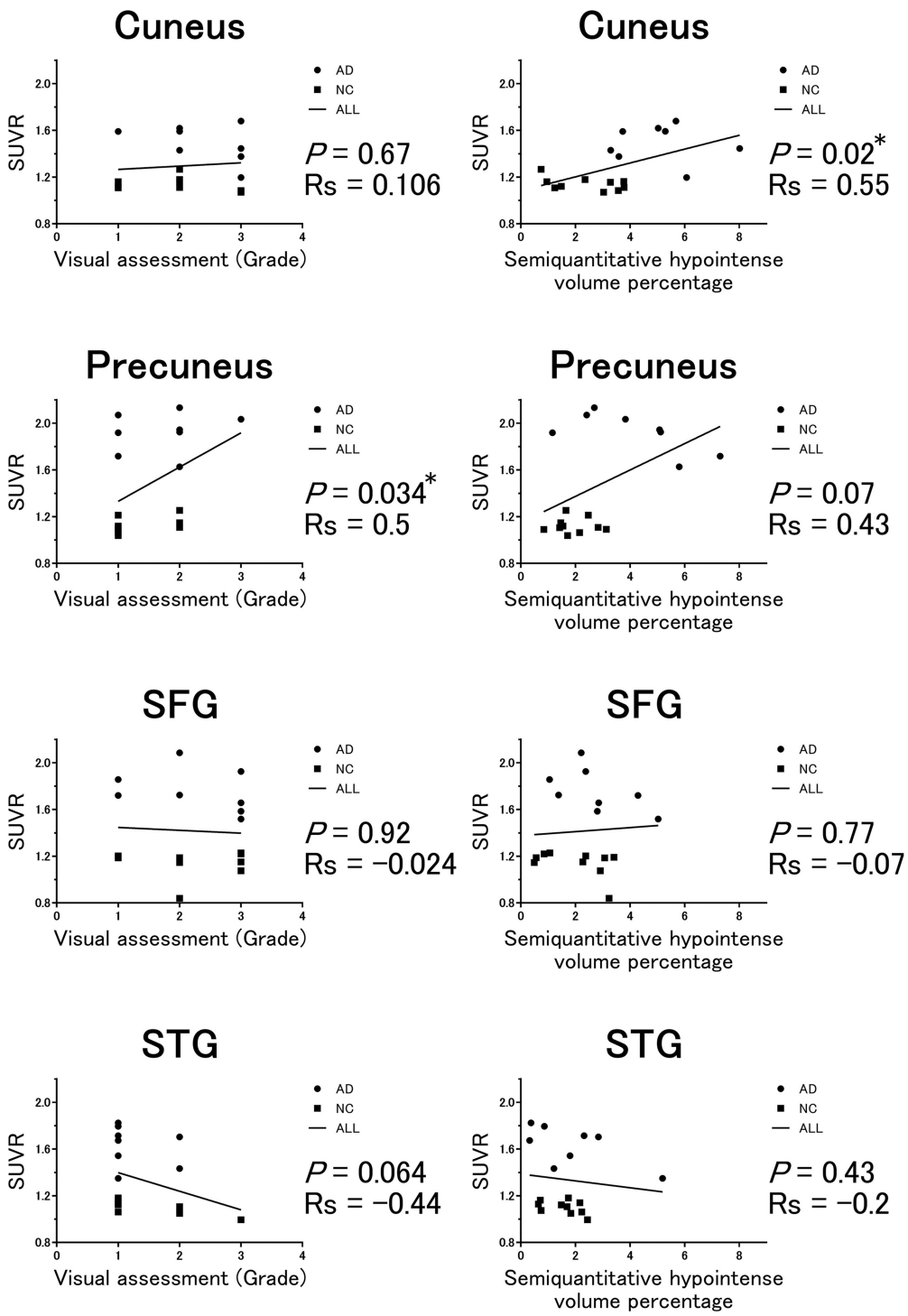

Fig. 5 A graph of correlations among the 4-point scale of PADRE images, the semiquantitative hypointense volume percentage of PADRE images, and SUVR of amyloid PET. The left column of the graph shows the correlations between the 4-point scale of PADRE images and SUVR of amyloid PET. The horizontal axis indicates the 4-point scale of PADRE images, and the vertical axis indicates the SUVR of amyloid PET. The right column of the graph shows the correlations between the semiquantitative hypointense volume percentage of PADRE images and SUVR of amyloid PET. The horizontal axis indicates the semiquantitative hypointense volume percentage, while the vertical axis indicates the SUVR of amyloid PET. *Indicating a statistical significance by Spearman's rank correlation. AD, Alzheimer's disease; NC, normal control; PADRE, phase difference enhanced; PET, positron emission tomography; SFG, superior frontal gyrus; STG, superior temporal gyrus; SUVR, standardized uptake value ratio.

iron of PADRE imaging may improve if PADRE imaging can stratify amyloid-β-related iron from age-, tau tangles-, and activated microglia-related iron by evaluating phase differences.

Using the phase-enhancing stratification method, the hypointense regions in the cerebral cortex of the PADRE imaging in the AD group were considered mainly reflecting amyloid-β-related iron but partially reflecting age-related iron, tau tangles-related iron, and activated microglia-related iron. A certain percentage of the AD group showed scarce hypointense regions in the cerebral cortex with grade 1 on the 4-point scale on PADRE imaging, although the AD group in the current study was positive for amyloid PET. In the AD group with grade 1 on the 4-point scale, only a few parts of amyloid-β-related iron in each ROI may be enhanced depending on the amount of the deposition of amyloid-β-, age-, tau tangles-, and activated microglia-related iron or the parameters of the PADRE sequences. In contrast, a certain percentage of the NC group showed hypointense regions in the cerebral cortex with grade 2 or 3 on the 4-point scale on PADRE imaging, although the NC group in the current study was negative for amyloid PET. Such hypointense areas in the NC group may reflect age-related iron, although no study has compared the hypointense areas of PADRE imaging with the pathology of the same area in human brain tissue. A previous histopathological study reported that iron deposition increased in the cerebral cortex with aging.[32] The amount of age-related iron deposition also differed depending on the brain regions.[43] To reduce the effect of age-related iron deposition regarding different ages or different brain regions, we evaluated the hypointense regions regarding the cuneus, precuneus, SFG, and STG, independently, for each subject. However, further optimization may be required to enhance only amyloid-β-related iron.

Similar to the current study, Tateishi et al.[28] also used the 4-point scale on PADRE imaging to assess the deposition of amyloid-β-related iron. They reported higher 4-point scaling grades for the AD group compared with the NC group, whereas the current study showed no significant differences in the 4-point scale evaluation in either region between the AD and NC groups. Furthermore, more than two-thirds of AD patients had hypointense areas in the cerebral cortex with grade 4 of the 4-point scale in the previous study, while no subjects had hypointense areas of grade 4 in the current study. A previous study used a 2D PADRE sequence, which generated noisier and thicker sliced images compared with a 3D PADRE sequence, which was used in the current study. Because the thick 2D PADRE images may include noise and blood vessels, as well as enhanced iron deposition, within each voxel, the 4-point scale of the 2D PADRE images may overestimate the deposition of amyloid-β-related iron. Because this study obtained only 3D PADRE images and not 2D PADRE images, we could not compare the 2D and 3D PADRE sequences; hence, validation of the usefulness of 2D and 3D PADRE sequences is warranted using amyloid PET. In contrast, this study performed a semiquantitative volumetric assessment to calculate the hypointense volume of PADRE imaging and showed that the volume percentage of hypointense areas within the cuneus and precuneus was significantly higher in the AD group than in the NC group. This method manually determined the threshold of the hypointense areas. Unlike QSM, PADRE imaging could not directly calculate the amount of iron deposition. Nonetheless, the semiquantitative volumetric assessment of amyloid-β-enhancing PADRE imaging could serve as a new technique in evaluating amyloid deposition.

This study has several limitations. First, this was a single-center study with a small number of cases. Furthermore, subjects with AD who were equivocal to negative for amyloid PET or NC subjects who were positive for amyloid PET were excluded. A larger study including subjects with various uptakes of amyloid PET is required. Second, only visual and semiquantitative assessments of PADRE images were performed in this study, and quantitative evaluation might reveal new aspects of the deposition of amyloid-β-related iron.

Conclusion

Amyloid-β-enhancing PADRE imaging and SUVR of amyloid PET showed a significant positive correlation in the cuneus and precuneus. Amyloid-β-enhancing PADRE imaging in the cuneus and precuneus may be useful for predicting the SUVR of amyloid PET.

Funding

This work was supported by JSPS KAKENHI (Grant Number JP 17K10415).

Conflicts of Interest

Tetsuya Yoneda received a research grant from Philips Healthcare. The other authors have no conflicts of interest.

Supplementary Information

Supplementary files below are available online.

Supplementary Fig. 1

The tissue probability map (TPM) corresponding to the segmented gray matter (GM) images is warped into the individual native space using nonlinear registration (Deformed TPM of GM images), creating a translation matrix. The automated anatomical labeling (AAL) brain atlas map in Montreal Neurological Institute (MNI) space is then nonlinearly warped into the individual native space by applying the translation matrix with the nearest-neighbor interpolation (Deformed AAL brain atlas map).

Supplementary Fig. 2

By applying a threshold of the probability = 0.7 to the deformed TPM of GM, an individual GM mask is created. We create an AAL atlas-based GM ROI by overlaying the GM mask on the deformed AAL brain atlas map. Then, unwanted phase, including partially contained white matter (WM) and vessels, is eliminated by additionally applying the PADRE mask. Finally, regions of WM and vessel mask were removed from the AAL atlas-based GM ROI, creating definitive atlas-based GM ROI.

Supplementary Fig. 3

The correlation between the 4-point scale and semiquantitative volume percentage of PADRE images. In the cuneus, a significant positive correlation is identified between the 4-point scale and semiquantitative volume percentage of PADRE images (Rs = 0.53, P = 0.02) in all subjects. In the precuneus, SFG, or STG, no significant correlations are identified between the 4-point scale and semiquantitative volume percentage of PADRE images (precuneus, Rs = 0.42, P = 0.08; SFG, Rs = –0.02, P = 0.94; STG, Rs = 0.24, P = 0.34).

References

1. Braak H, Braak E. Neuropathological stageing of Alzheimer-related changes. Acta Neuropathol 1991; 82:239–259.
2. Jack CR, Bennett DA, Blennow K, et al. NIA-AA Research Framework: Toward a biological definition of Alzheimer's disease. Alzheimer's & Dementia 2018; 14:535–562.
3. Ikonomovic MD, Klunk WE, Abrahamson EE, et al. Post-mortem correlates of in vivo PiB-PET amyloid imaging in a typical case of Alzheimer's disease. Brain 2008; 131:1630–1645.
4. Fleisher AS, Chen K, Liu X, et al. Using positron emission tomography and florbetapir F18 to image cortical amyloid in patients with mild cognitive impairment or dementia due to Alzheimer disease. Arch Neurol 2011; 68:1404–1411.
5. Clark CM, Pontecorvo MJ, Beach TG, et al. AV-45-A16 Study Group. Cerebral PET with florbetapir compared with neuropathology at autopsy for detection of neuritic amyloid-β plaques: a prospective cohort study. Lancet Neurol 2012; 11:669–678.
6. Clark CM, Schneider JA, Bedell BJ, et al. AV45-A07 Study Group. Use of florbetapir-PET for imaging beta-amyloid pathology. JAMA 2011; 305:275–283.
7. Ossenkoppele R, Jansen WJ, Rabinovici GD, et al. Prevalence of amyloid PET positivity in dementia syndromes: a meta-analysis. JAMA 2015; 313:1939–1949.
8. Shea YF, Barker W, Greig-Gusto MT, Loewenstein DA, Duara R, DeKosky ST. Impact of amyloid PET imaging in the memory clinic: A systematic review and meta-analysis. J Alzheimers Dis 2018; 64:323–335.
9. Telling ND, Everett J, Collingwood JF, et al. Iron biochemistry is correlated with amyloid plaque morphology in an established mouse model of Alzheimer's disease. Cell Chem Biol 2017; 24:1205–1215.e1–e3.
10. Lovell MA, Robertson JD, Teesdale WJ, Campbell JL, Markesbery WR. Copper, iron and zinc in Alzheimer's disease senile plaques. J Neurol Sci 1998; 158:47–52.
11. Wu CW, Liao PC, Yu L, et al. Hemoglobin promotes Abeta oligomer formation and localizes in neurons and amyloid deposits. Neurobiol Dis 2004; 17:367–377.
12. van Rooden S, Maat-Schieman ML, Nabuurs RJ, et al. Cerebral amyloidosis: postmortem detection with human 7.0-T MR imaging system. Radiology 2009; 253:788–796.
13. Benveniste H, Einstein G, Kim KR, Hulette C, Johnson GA. Detection of neuritic plaques in Alzheimer's disease by magnetic resonance microscopy. Proc Natl Acad Sci U S A 1999; 96:14079–14084.
14. Jack CR, Garwood M, Wengenack TM, et al. In vivo visualization of Alzheimer's amyloid plaques by magnetic resonance imaging in transgenic mice without a contrast agent. Magn Reson Med 2004; 52:1263–1271.
15. Chamberlain R, Reyes D, Curran GL, et al. Comparison of amyloid plaque contrast generated by T2-weighted, T2*-weighted, and susceptibility-weighted imaging methods in transgenic mouse models of Alzheimer's disease. Magn Reson Med 2009; 61:1158–1164.
16. Gong NJ, Dibb R, Bulk M, van der Weerd L, Liu C. Imaging beta amyloid aggregation and iron accumulation in Alzheimer's disease using quantitative susceptibility mapping MRI. Neuroimage 2019; 191:176–185.
17. van Bergen JM, Li X, Hua J, et al. Colocalization of cerebral iron with amyloid beta in mild cognitive impairment. Sci Rep 2016; 6:35514.
18. Ayton S, Fazlollahi A, Bourgeat P, et al. Australian Imaging Biomarkers and Lifestyle (AIBL) Research Group, Salvado O, Bush AI. Cerebral quantitative susceptibility mapping predicts amyloid-β-related cognitive decline. Brain 2017; 140:2112–2119.
19. van Bergen JMG, Li X, Quevenco FC, et al. Simultaneous quantitative susceptibility mapping and flutemetamol-PET suggests local correlation of iron and β-amyloid as an indicator of cognitive performance at high age. Neuroimage 2018; 174:308–316.
20. Tiepolt S, Schäfer A, Rullmann M, et al. Quantitative susceptibility mapping of amyloid-β aggregates in Alzheimer's disease with 7T MR. J Alzheimers Dis 2018; 64:393–404.
21. Cogswell PM, Wiste HJ, Senjem ML, et al. Associations of quantitative susceptibility mapping with Alzheimer's disease clinical and imaging markers. Neuroimage 2021; 224:117433.
22. Kakeda S, Korogi Y, Yoneda T, et al. A novel tract imaging technique of the brainstem using phase difference enhanced imaging: normal anatomy and initial experience in multiple system atrophy. Eur Radiol 2011; 21:2202–2210.
23. Doishita S, Sakamoto S, Yoneda T, et al. Differentiation of brain metastases and gliomas based on color map of phase difference enhanced imaging. Front Neurol 2018; 9:788.
24. Futatsuya K, Kakeda S, Yoneda T, et al. Juxtacortical lesions in multiple sclerosis: Assessment of gray matter involvement using phase difference-enhanced imaging (PADRE). Magn Reson Med Sci 2016; 15:349–354.
25. Kakeda S, Yoneda T, Ide S, et al. Zebra sign of precentral gyri in amyotrophic lateral sclerosis: A novel finding using phase difference enhanced (PADRE) imaging-initial results. Eur Radiol 2016; 26:4173–4183.

26. Miyata M, Kakeda S, Yoneda T, et al. Signal intensity of cerebral gyri in corticobasal syndrome on phase difference enhanced magnetic resonance images: Comparison of progressive supranuclear palsy and Parkinson's disease. J Neurol Sci 2020; 419:117210.
27. Yoneda T, Hashimoto K, Kuniyasu A, et al. Statistical phase noise elimination for amyloid plaque detection. Proceedings of the 23rd Annual Meeting of ISMRM, Toronto, 2015; 2223.
28. Tateishi M, Kitajima M, Hirai T, et al. Differentiating between Alzheimer disease patients and controls with phase-difference-enhanced imaging at 3T: A feasibility study. Magn Reson Med Sci 2018; 17:283–292.
29. McKhann G, Drachman D, Folstein M, Katzman R, Price D, Stadlan EM. Clinical diagnosis of Alzheimer's disease: report of the NINCDS-ADRDA Work Group under the auspices of Department of Health and Human Services Task Force on Alzheimer's disease. Neurology 1984; 34:939–944.
30. Rolls ET, Joliot M, Tzourio-Mazoyer N. Implementation of a new parcellation of the orbitofrontal cortex in the automated anatomical labeling atlas. Neuroimage 2015; 122:1–5.
31. Ide S, Kakeda S, Korogi Y, et al. Delineation of optic radiation and stria of Gennari on high-resolution phase difference enhanced imaging. Acad Radiol 2012; 19:1283–1289.
32. HALLGREN B, SOURANDER P. The effect of age on the non-haemin iron in the human brain. J Neurochem 1958; 3:41–51.
33. Choi WH, Um YH, Jung WS, Kim SH. Automated quantification of amyloid positron emission tomography: a comparison of PMOD and MIMneuro. Ann Nucl Med 2016; 30:682–689.
34. Wong DF, Rosenberg PB, Zhou Y, et al. In vivo imaging of amyloid deposition in Alzheimer disease using the radioligand ^{18}F-AV-45 (florbetapir F 18). J Nucl Med 2010; 51:913–920.
35. Forsberg A, Engler H, Almkvist O, et al. PET imaging of amyloid deposition in patients with mild cognitive impairment. Neurobiol Aging 2008; 29:1456–1465.
36. Palmqvist S, Schöll M, Strandberg O, et al. Earliest accumulation of β-amyloid occurs within the default-mode network and concurrently affects brain connectivity. Nat Commun 2017; 8:1214.
37. van Duijn S, Bulk M, van Duinen SG, et al. cortical iron reflects severity of Alzheimer's disease. J Alzheimers Dis 2017; 60:1533–1545.
38. Spotorno N, Acosta-Cabronero J, Stomrud E, et al. Relationship between cortical iron and tau aggregation in Alzheimer's disease. Brain 2020; 143:1341–1349.
39. Ayton S, Wang Y, Diouf I, et al. Brain iron is associated with accelerated cognitive decline in people with Alzheimer pathology. Mol Psychiatry 2020; 25:2932–2941.
40. Bulk M, Kenkhuis B, van der Graaf LM, Goeman JJ, Natté R, van der Weerd L. Postmortem T2*- weighted MRI imaging of cortical iron reflects severity of Alzheimer's disease. J Alzheimers Dis 2018; 65:1125–1137.
41. Zeineh MM, Chen Y, Kitzler HH, Hammond R, Vogel H, Rutt BK. Activated iron-containing microglia in the human hippocampus identified by magnetic resonance imaging in Alzheimer disease. Neurobiol Aging 2015; 36:2483–2500.
42. Smith MA, Harris PL, Sayre LM, Perry G. Iron accumulation in Alzheimer disease is a source of redox-generated free radicals. Proc Natl Acad Sci U S A 1997; 94:9866–9868.
43. Chen L, Soldan A, Oishi K, et al. Quantitative susceptibility mapping of brain iron and β-amyloid in MRI and PET relating to cognitive performance in cognitively normal older adults. Radiology 2021; 298:353–362.